ChemComm

COMMUNICATION

View Article Online
View Journal | View Issue

Cite this: *Chem. Commun.*, 2020, **56**, 13872

Received 15th September 2020,
Accepted 28th September 2020

DOI: 10.1039/d0cc06222g

rsc.li/chemcomm

Monodisperse CoSb nanocrystals as high-performance anode material for Li-ion batteries†

Shutao Wang, ‡[ab] Meng He,[ab] Marc Walter,[ab] Kostiantyn V. Kravchyk *[ab] and Maksym V. Kovalenko *[ab]

Towards enhancement of the power density of Li-ion batteries (LIBs), antimony-based intermetallic compounds have recently attracted considerable attention as compelling anode materials owing to their high rate capability as compared to state-of-the-art graphite anodes. Here we report a facile colloidal synthesis of monodisperse CoSb nanocrystals (NCs) as a model intermetallic anode material for LIBs *via* the reaction between Co NCs and $SbCl_3$ in oleylamine under reducing conditions. We found that *ca.* 20 nm CoSb NCs exhibit enhanced cycling stability as compared to larger *ca.* 40 nm CoSb NCs and Sb NCs with size on the order of 20 nm.

Lithium-ion batteries (LIBs) are the most common secondary electrochemical energy storage systems, being a key component of portable electronics and electric mobility.[1] Further improvement of the power density of the state-of-the-art LIBs might be accomplished by the replacement of the graphite anode, which has a moderate rate capability.[2–4] Specifically, due to the low lithiation/delithiation potentials of graphite, lithium plating on the graphite electrode becomes thermodynamically favorable upon fast charging, eventually resulting in short circuit and cell failure.[5,6] In this context, the last two decades have seen a surge of reports on various alternative-to-graphite anode materials with higher rate capability and stable cycling performance.[7] Of all studied anodes for LiBs, Sb is one of the most appealing candidates for replacing graphite due to its superior rate capability and high charge storage capacity of 660 mA h g^{-1} (7246 mA h cm^{-3}).[8] However, harnessing the electrochemical lithiation of Sb is hampered by its low capacity retention caused by massive volume variations (*ca.* 150%) upon alloying/dealloying reactions.[9] These volume changes lead to active-material particle pulverization, the formation of cracks in the rigid solid–electrolyte interface as well as mechanical disintegration of the electrodes from the current collector. These issues can be mitigated by nanostructuring of Sb and its embedding into an elastic and conductive network.[10,11] For instance, the cycling stability of electrodes comprising 20 nm Sb NCs was shown to be superior over microcrystalline (bulk) Sb particles.[12] Besides nanostructuring, an effective strategy is the employment of intermetallic compounds comprising electroactive Sb and inactive (Fe,[13] Co,[14,15] Ni,[16] Cu[17]) metal components with regard to Li. Enhanced cycling stability of such alloys is assigned to the presence of an inactive metal matrix that buffers the volume variations of Sb upon cycling and thus hampers their electrochemical aggregation. It should be noted, however, that although nanostructured intermetallic compounds can serve as excellent model systems, they might be prohibitively expensive for practical application in commercial batteries.

In this work, we were motivated to employ Sb based alloy-type compounds with an electrochemically non-active Co metal such as CoSb in combination with a nanostructuring approach. We then aimed to discover whether the cycling stability of CoSb nanocrystals (NCs) changes with the size and they exhibit advantageous cycling behavior compared to elemental Sb NCs of the same size. The underlying chemistry used in this work was based on the sequential reduction of cobalt(II) and antimony(III) from their transient oleylamide complexes. The formation of such complexes is promoted with the secondary ammonium base, $LiN(iPr)_2$.[18] We find that *ca.* 20 nm CoSb NCs demonstrate superior cycling stability over larger *ca.* 40 nm CoSb NCs and pure *ca.* 20 nm Sb NCs, delivering an initial charge capacity of 544 mA h g^{-1} with a capacity retention of 82% after 1000 cycles at a current density of 660 mA g^{-1}.

In the one-pot synthesis of CoSb NCs (Fig. 1a), first, oleylamine was mixed with $CoCl_2$, followed by the injection of $LiN(iPr)_2$ (solved in oleylamine) at 270 °C, and 30 s later at 235 °C, injection of $SbCl_3$ (solved in toluene/1-octadecene) into

[a] *Laboratory of Inorganic Chemistry, Department of Chemistry and Applied Biosciences, ETH Zürich, Vladimir-Prelog-Weg 1, Zürich CH-8093, Switzerland. E-mail: kravchyk@inorg.chem.ethz.ch, mvkovalenko@ethz.ch*

[b] *Laboratory for Thin Films and Photovoltaics, Empa – Swiss Federal Laboratories for Materials Science and Technology, Überlandstrasse 129, Dübendorf CH-8600, Switzerland*

† Electronic supplementary information (ESI) available. See DOI: 10.1039/d0cc06222g

‡ Present address: Department of Chemistry, University College London, 20 Gordon Street, London, WC1H 0AJ, UK.

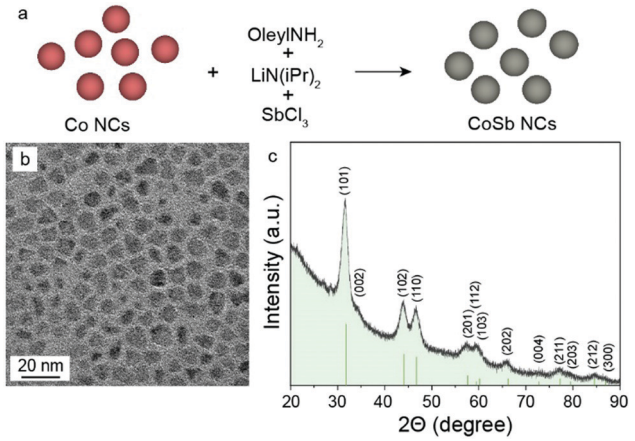

Fig. 1 (a) Schematic illustration of the one-pot synthesis of CoSb NCs, along with corresponding (b) TEM image and (c) powder XRD pattern of CoSb NCs.

the solution. Afterward, the reaction mixture was maintained at *ca.* 235 °C for an additional 4 h to form homogeneous CoSb NCs. In this synthesis, $LiN(iPr)_2$ acted as a mild base for the partial deprotonation of oleylamine, thereby fostering the formation of highly reactive metal–oleylamido species. The latter complexes instantaneously decompose, causing a nucleation burst, resulting in the formation of CoSb NCs.

Detailed characterization of the synthesized CoSb NCs by transmission electron microscopy (TEM, Fig. 1b), electron diffraction (Fig. S1a–d, ESI†), and powder X-ray diffraction (XRD, Fig. 1c), confirmed the formation of chemically pure, highly crystalline hexagonal CoSb NCs (Fig. 1c, space group *P*63/*mmc*, $a = b = 3.88$ Å, $c = 5.185$ Å, JCPDS No. 033-0097). The resulting size of CoSb NCs can be tuned in the range of 5–45 nm by varying the reaction time, temperature, and quantity of precursors (Fig. S1a–d, S2a and Table S1, ESI†). By doubling the molar amount of $SbCl_3$ with respect to $CoCl_2$, crystalline $CoSb_2$ NCs were obtained (Fig. S1e–g, S2b and Table S2, ESI†). Aiming to compare the electrochemical performance of CoSb with pure Sb, monodisperse Sb NCs were also synthesized using a previously published procedure (Fig. S1h, ESI†).[19]

After the synthesis of CoSb NCs, $CoSb_2$ NCs, and Sb NCs, insulating organic capping ligands were removed by a hydrazine-based ligand-stripping procedure, similar to that used for colloidal quantum dots.[20] For the electrochemical measurements, the electrodes were prepared by mixing powders of the corresponding NCs with carbon black (CB), carboxymethyl cellulose (CMC), and water. The resulting slurries were cast onto a copper current collector (see ESI,† for details). Importantly, ligand-removal and mechanical mixing did not lead to any noticeable changes in the size and morphology of NCs (Fig. S3, ESI†). Before measurements, the electrodes were dried for 6 h at room temperature and then for 12 h at 80 °C under vacuum before transferring into the Ar-filled glove box. The same active material mass loading of ~ 0.5 mg cm^{-2} was used for electrodes to minimize the effect of the different electrode mass loading on the cycling capability.

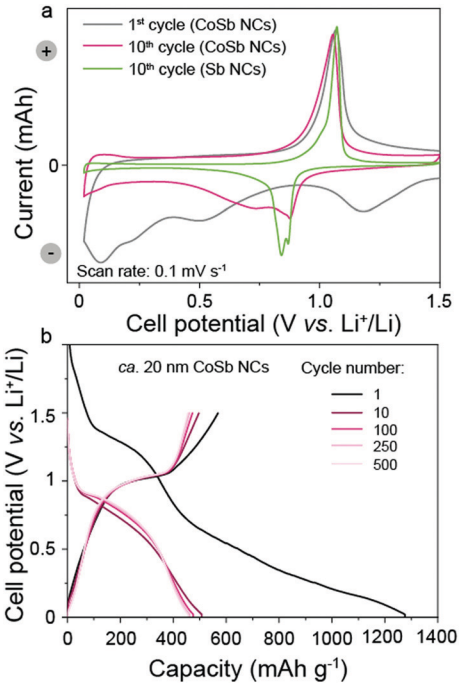

Fig. 2 (a) Cyclic voltammetry and (b) galvanostatic charge–discharge curves of *ca.* 20 nm CoSb NCs measured at a scan rate of 0.1 mV s^{-1} and current density of 660 mA g^{-1}, respectively (cyclic voltammetry curve of *ca.* 20 nm Sb NCs is given for comparison). See also Fig. S5 (ESI†) for galvanostatic charge–discharge curves of *ca.* 20 nm Sb NCs.

Coin-type cells were employed for the electrochemical tests. The cell consisted of lithium foil as the counter and the reference electrode, the working electrode comprising the corresponding NCs, and a glass-fiber separator that was placed between both electrodes and soaked with the lithium electrolyte (1 M $LiPF_6$ in ethylene carbonate/dimethyl carbonate +3 wt% of fluoroethylene carbonate).

Fig. 2a shows cyclic voltammetry (CV) curves of CoSb NCs and Sb NCs at a scan rate of 0.1 mV s^{-1}. In the first cathodic cycle (lithiation step), a small broad peak at about 1.2 V *vs.* Li^+/Li was attributed to the formation of a solid–electrolyte interphase (SEI) layer due to the irreversible reduction of the electrolyte during the first cycle. Upon further lithiation, a reduction peak at 0.5 V (*vs.* Li^+/Li) appeared, which was ascribed to lithium insertion into CoSb, forming a Li_2Sb alloy and a metallic Co phase. Continued lithiation resulted in the appearance of a peak at 0.2 V *vs.* Li^+/Li, evidencing the formation of Li_3Sb alloy. A broad peak at 0.1 V *vs.* Li^+/Li can be attributed to the lithiation of the CB. In the reverse scan, the CoSb electrode displayed only one pronounced peak at 1.07 V *vs.* Li^+/Li, which can be ascribed to delithiation of Li_3Sb. Upon further cathodic cycling, two peaks associated with Li_2Sb and Li_3Sb formation were shifted to higher voltages of 0.88 V and 0.73 V *vs.* Li^+/Li, respectively (see Fig. S4 (ESI†) for a full set of CV cycles). The CV curve of Sb NCs was similar to the CV curve of CoSb NCs, showing a two-step lithiation reaction resulting in the formation of Li_2Sb and Li_3Sb alloys (0.88 V and 0.84 V *vs.* Li^+/Li) and a one-step delithiation reaction (1.07 V *vs.* Li^+/Li).

It should be noted that numerous earlier *in situ* XRD measurements[21] confirm the formation of Li_2Sb and Li_3Sb alloys within the given voltage range of 0.9 to 0.7 V *vs.* Li^+/Li, which is also in agreement with theoretical calculations by Huggins.[22] The galvanostatic discharge and charge profiles of CoSb NCs measured at a current density of 660 mA h g^{-1} (1C for Sb NCs) were characterized by broad plateaus (Fig. 2b), in good agreement with CoSb CV curves. The smooth shape of the galvanostatic voltage profiles, as well as the broad width of CV curves for electrodes composed of CoSb NCs suggest a slow and gradual lithiation of CoSb NCs. In fact, such behavior with spread-out features in the CV curves and galvanostatic voltage profiles is rather usual for nanostructured materials, as often reported in the past.[23]

As determined by galvanostatic cycling measurements of CoSb NC and Sb NC performed at 660 mA g^{-1}, Sb NCs delivered higher capacities in the first 250 cycles as compared to CoSb NCs (Fig. 3a). However, upon prolonged cycling for 1000 cycles, the capacity of Sb NCs gradually decreased. Conversely, the capacities of the CoSb NCs were stable for 1000 cycles, with a high capacity retention of 82%. In both cases, the coulombic efficiency was initially low, but increased to more than 99.54% and 99.92% for Sb NCs and CoSb NCs, respectively. Notably, a wide range of prelithiation materials can be employed to compensate for the initial lithium losses in the electrodes composed of Sb NCs and CoSb NCs. Typical prelithiation materials are stabilized lithium metal and lithium silicide on the anode side or binary lithium compounds (*e.g.*, Li_2O, LiF and Li_3N) on the cathode side of LIBs, respectively.[24] The cycling stability tests of half-cells employing CoSb NCs at a high current density of 2640 mA g^{-1} showed high capacity retention of 89%. Only 13% of initial charge storage capacity was retained in the case of Sb NCs.

Notably, we have also tested the electrochemical performance of CoSb NCs with smaller and larger sizes on the order of 5 and 40 nm (Fig. 3c). The electrode composed of *ca.* 40 nm CoSb NCs showed systematically higher initial capacities for the first 100 cycles than the one composed of small NCs. However, upon prolonged cycling, the capacity of the large CoSb NCs gradually decreased. The capacity of *ca.* 5 nm CoSb NCs was slightly lower than that of *ca.* 20 nm CoSb NCs. This difference can be explained by the presence of a higher amount of the amorphous surface oxide shell on the smaller *ca.* 5 nm CoSb NCs. The latter leads to the formation of Li_2O, eventually resulting in a higher irreversible capacity loss in the first discharge cycle as compared to larger *ca.* 20 nm CoSb NCs.

In an effort to unveil the favorable composition of Co–Sb alloys, $CoSb_2$ NCs on the order of 20 nm were also tested (Fig. S6, ESI†). It has been revealed that although $CoSb_2$ electrodes yielded a higher capacity of 620 mA h g^{-1}, their cycling behavior was similar to pure Sb NCs. In particular, the capacity of $CoSb_2$ NCs sharply decayed over 100 cycles. Apparently, we speculate that a higher amount of Co in the Co–Sb alloy helps reduce the anisotropic mechanical stress within the electrode upon their lithiation/delithiation, eventually resulting in enhanced cycling stability of CoSb over $CoSb_2$ alloys.

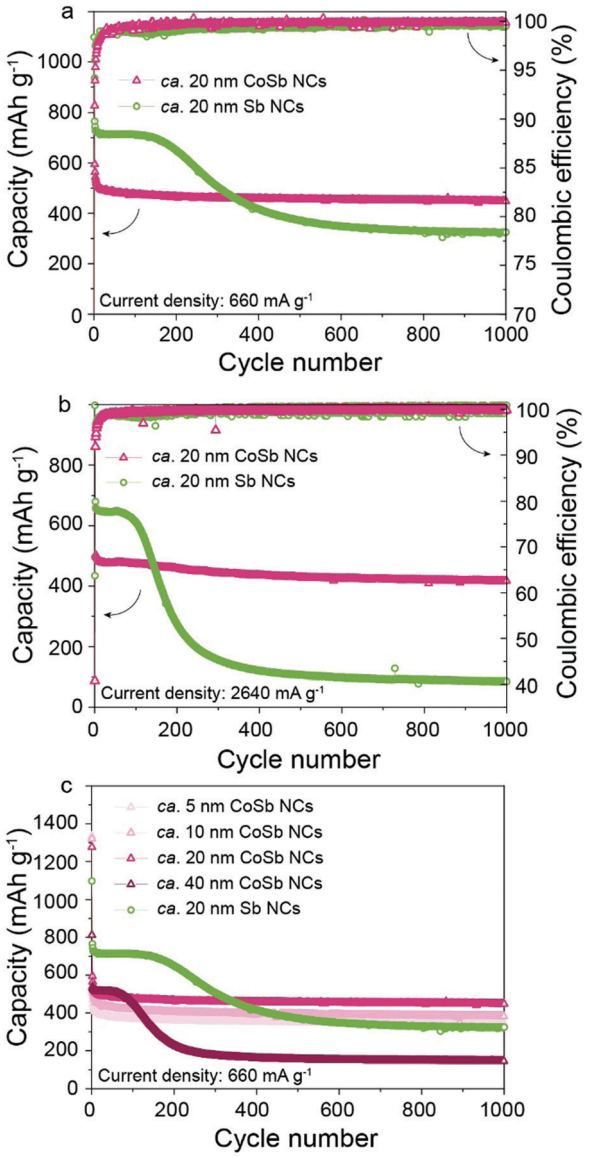

Fig. 3 (a and b) Comparison of the cycling stability of CoSb NCs and Sb NCs, all with *ca.* 20 nm mean particle size, in Li-ion half-cells at a current density of 660 mA g^{-1} and 2640 mA g^{-1}. (c) Cycling stability of electrodes composed of CoSb NCs of various sizes (*ca.* 5 to 40 nm) and *ca.* 20 nm Sb NCs. All cells were cycled at room temperature in the potential range of 0.02–1.5 V *vs.* Li^+/Li. The initially higher capacity of CoSb NCs and Sb NCs as compared to their theoretical values of 445 mA h g^{-1} and 660 mA h g^{-1} is attributed to the additional contribution of CB to the measured charge storage capacity.

Aiming to identify the structural evolution of the CoSb NC electrodes upon electrochemical cycling, *ex situ* XRD measurements were performed (Fig. 4). A steady decrease in the intensity of the CoSb diffraction peaks and a concomitant peak broadening indicated that the cycling of CoSb NCs occurs with concomitant size reduction and amorphization of the material. Complete amorphization of the material takes place after 100 cycles. Interestingly, similar amorphization behavior was also observed for pure Sb NCs during cycling (Fig. S7, ESI†). We speculate that the *in situ* formation of the amorphous CoSb

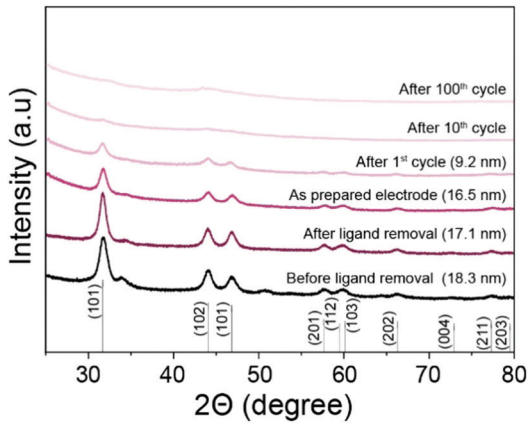

Fig. 4 XRD patterns of CoSb NCs before and after ligand removal, after electrode preparation, and after 1st, 10th, and 100th cycles. The mean crystallite size of NCs was determined by Rietveld refinement from XRD patterns.

during cycling might allow the structural integrity of the electrodes to be maintained and strongly mitigate their undergoing large mechanical stress during lithiation of the Sb phase. This eventually results in a reduction of the amount of anisotropic mechanical stress within the electrode. Notably, *ex situ* XRD measurements indicate that Co-domains are not fully inactive after the first lithiation, but take part in full CoSb recovery. It should be pointed out that high cycling stability of *ca.* 20 nm CoSb NCs might also be attributed to their small size, which allows mitigating their fracturing upon cycling.[25–27]

In summary, we have developed a simple colloidal synthesis of highly uniform CoSb NCs by sequential reduction of cobalt(II) and antimony(III)oleylamine, promoted by the formation of metal–olyelamido complexes. A side-by-side comparison of CoSb NCs of different sizes on the order of 5 to 40 nm showed that the charge storage capacity and cycling stability of *ca.* 20 nm CoSb NCs are superior to those of smaller and larger CoSb NCs and Sb NCs of the same size. Specifically, *ca.* 20 nm CoSb NCs delivered a stable average capacity of 448 mA h g^{-1} for 1000 cycles at a high density of 660 mA g^{-1}. In contrast, the charge storage capacity of large *ca.* 40 nm CoSb NCs and *ca.* 20 nm Sb NCs gradually decayed after 100–150 cycles. The capacities of *ca.* 5 nm CoSb NCs was stable over cycling, but lower than for *ca.* 20 nm CoSb NCs as a result of a high amount of the amorphous surface oxide shell. Further work is needed to understand the superior cycling stability of *ca.* 20 nm CoSb NCs, which can presumably be attributed to the presence of *in situ* formed Co nano-domains, which act as a matrix that buffers the volumetric changes occurring during lithiation/delithiation, and prevents the electrochemical aggregation of Sb NCs.

This research is part of the activities of SCCER HaE, which is financially supported by the Innosuisse – Swiss Innovation Agency. The authors are grateful to the research facilities of ETH Zürich (ETH Electron Microscopy Center, Department of Chemistry and Applied Biosciences) and Empa (Empa Electron Microscopy Center) for access to the instruments and for technical assistance.

Conflicts of interest

There are no conflicts to declare.

Notes and references

1 J. Xie and Y.-C. Lu, *Nat. Commun.*, 2020, **11**, 2499.
2 J. Billaud, F. Bouville, T. Magrini, C. Villevieille and A. R. Studart, *Nat. Energy*, 2016, **1**, 16097.
3 Y. Liu, Z. Sun, X. Sun, Y. Lin, K. Tan, J. Sun, L. Liang, L. Hou and C. Yuan, *Angew. Chem., Int. Ed.*, 2020, **59**, 2473–2482.
4 Y. Zhang, Z. Wang, F. U. Zaman, Z. Zhao, X. Sun, J. Zhang, L. Hou and C. Yuan, *J. Mater. Chem. A*, 2019, **7**, 3264–3277.
5 K.-H. Chen, M. J. Namkoong, V. Goel, C. Yang, S. Kazemiabnavi, S. M. Mortuza, E. Kazyak, J. Mazumder, K. Thornton, J. Sakamoto and N. P. Dasgupta, *J. Power Sources*, 2020, **471**, 228475.
6 J. Kasnatscheew, T. Placke, B. Streipert, S. Rothermel, R. Wagner, P. Meister, I. C. Laskovic and M. Winter, *J. Electrochem. Soc.*, 2017, **164**, A2479–A2486.
7 N. Nitta, F. Wu, J. T. Lee and G. Yushin, *Mater. Today*, 2015, **18**, 252–264.
8 Z. Liu, T. Song and U. Paik, *J. Mater. Chem. A*, 2018, **6**, 8159–8193.
9 S. Liang, Y.-J. Cheng, J. Zhu, Y. Xia and P. Müller-Buschbaum, *Small Methods*, 2020, **4**, 2000218.
10 R. J. C. Dubey, P. V. W. Sasikumar, N. Cerboni, M. Aebli, F. Krumeich, G. Blugan, K. V. Kravchyk, T. Graule and M. V. Kovalenko, *Nanoscale*, 2020, **12**, 13540–13547.
11 J. Tian, H. Yang, C. Fu, M. Sun, L. Wang and T. Liu, *Compos. Commun.*, 2020, **17**, 177–181.
12 M. He, K. Kravchyk, M. Walter and M. V. Kovalenko, *Nano Lett.*, 2014, **14**, 1255–1262.
13 C. Villevieille, C. M. Ionica-Bousquet, B. Fraisse, D. Zitoun, M. Womes, J. C. Jumas and L. Monconduit, *Solid State Ionics*, 2011, **192**, 351–355.
14 J. Xie, G. S. Cao, X. B. Zhao, M. J. Zhao, Y. D. Zhong, L. Z. Deng, Y. H. Guan and Z. T. Wu, *J. Mater. Sci.*, 2004, **39**, 1105–1107.
15 J. Zhu, T. Sun, J. Chen, W. Shi, X. Zhang, X. Lou, S. Mhaisalkar, H. H. Hng, F. Boey, J. Ma and Q. Yan, *Chem. Mater.*, 2010, **22**, 5333–5339.
16 R. Chen, X. Xue, J. Lu, T. Chen, Y. Hu, L. Ma, G. Zhu and Z. Jin, *Nanoscale*, 2019, **11**, 8803–8811.
17 C. Zhang, K.-Q. Xu, W. Zhou, X.-F. Lu, R.-Y. Li and G.-R. Li, *Part. Part. Syst. Charact.*, 2016, **33**, 553–559.
18 M. He, L. Protesescu, R. Caputo, F. Krumeich and M. V. Kovalenko, *Chem. Mater.*, 2015, **27**, 635–647.
19 M. Walter, R. Erni and M. V. Kovalenko, *Sci. Rep.*, 2015, **5**, 8418.
20 D. V. Talapin and C. B. Murray, *Science*, 2005, **310**, 86–89.
21 C. Villevieille, M. Ebner, J. L. Gómez-Cámer, F. Marone, P. Novák and V. Wood, *Adv. Mater.*, 2015, **27**, 1676–1681.
22 J. Wang, I. D. Raistrick and R. A. Huggins, *J. Electrochem. Soc.*, 1986, **133**, 457–460.
23 S. Goriparti, E. Miele, F. D. Angelis, E. D. Fabrizio, R. P. Zaccaria and C. Capiglia, *J. Power Sources*, 2014, **257**, 421–443.
24 Y. Sun, Y. Li, J. Sun, Y. Li, A. Pei and Y. Cui, *Energy Storage Mater.*, 2017, **6**, 119–124.
25 L. Xu, C. Kim, A. K. Shukla, A. Dong, T. M. Mattox, D. J. Milliron and J. Cabana, *Nano Lett.*, 2013, **13**, 1800–1805.
26 P.-C. Tsai, B. Wen, M. Wolfman, M.-J. Choe, M. S. Pan, L. Su, K. Thornton, J. Cabana and Y.-M. Chiang, *Energy Environ. Sci.*, 2018, **11**, 860–871.
27 H. Liu, M. Wolf, K. Karki, Y.-S. Yu, E. A. Stach, J. Cabana, K. W. Chapman and P. J. Chupas, *Nano Lett.*, 2017, **17**, 3452–3457.